Uranium speciation control by uranyl sulfate and phosphate in tailings subject to a Sahelian climate, Cominak, Niger

Florian Lahrouch [a,*], Benoit Baptiste [a], Kathy Dardenne [b], Jörg Rothe [b], Erik Elkaim [c], Michael Descostes [d,e], Martine Gerard [a,**]

[a] *Sorbonne Université, CNRS UMR7590, MNHN, IRD, Institut de Minéralogie, de Physique des Matériaux et de Cosmochimie (IMPMC), 4 Place Jussieu, Paris, F- 75005, France*
[b] *Karlsruhe Institute of Technology, Institute for Nuclear Waste Disposal (INE), P.O. Box 3640, Karlsruhe, D-76021, Germany*
[c] *Synchrotron SOLEIL, L'Orme des Merisiers, Saint-Aubin, BP 48, Gif-sur-Yvette Cedex, F-91192, France*
[d] *ORANO Mines, Environmental R & D Department, 125 Avenue de Paris, Châtillon, F-93320, France*
[e] *Centre de Géosciences, MINES ParisTech, PSL University, 35 rue St Honoré, Fontainebleau, 77300, France*

HIGHLIGHTS

- Sulfate and phosphate groups control U mobility in the tailings environment.
- Neoformation of uranyl sulfates is favored by evapotranspiration phenomena.
- Uranyl phosphate minerals are efficient traps for uranium long-term mobility.
- Inherited U(IV) phases included in quartz are identified in tailings.

GRAPHICAL ABSTRACT

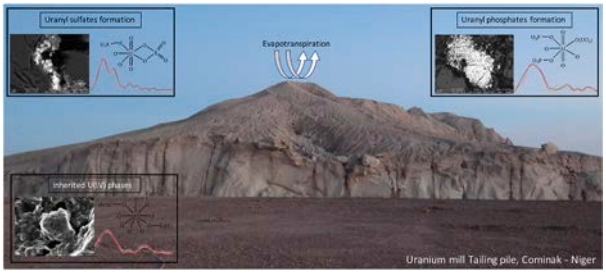

ARTICLE INFO

Handling Editor: Milena Horvat

Keywords:
Uranium
Mining wastes
Uranium migration
EXAFS spectroscopy
Environment
Uranyl phosphate
Uranyl sulfate

ABSTRACT

Long-term uranium mobility in tailings is an environmental management issue. The present study focuses on two U-enriched layers, surficial and buried 14.5 m, of the tailings pile of Cominak, Niger. The acidic and oxidizing conditions of the tailings pile combined with evapotranspiration cycles related to the Sahelian climate control U speciation. Uraninite, brannerite, and moluranite as well as uranophane are relict U phases. EXAFS spectroscopy, HR-XRD, and SEM/WDS highlight the major role of uranyl sulfate groups in uranium speciation. Uranyl phosphate neoformation in the buried layer (paleolayer) acts as an efficient trap for uranium.

* Corresponding authors.
** Corresponding author.
E-mail addresses: florian.lahrouch@upmc.fr (F. Lahrouch), martine.gerard@sorbonne-universite.fr (M. Gerard).

1. Introduction

Tailing management related to uranium mining activity raises environmental concern among governmental authorities and mining companies regarding the long-term mobility of radioactive elements. The tailings generated by uranium extraction consist of residual ore minerals. The uranium extraction yield generally around 95% related to the milling process and ore mineralogy (Chautard et al., 2020), and by consequence, the uranium concentration in the tailings is rather low. The residual uranium still present in the tailings, composed of U-238, U-235 and U-234 (half-lives of 4.5 billion years, 703 million years and 245 thousand years, respectively), is a possible source of radioactive contamination. The long-term management of a large quantity of U-tailings, approximately 2 billion tons in the world (Steinhausler and Zaitseva, 2007), remains an environmental management issue. However, nearly 50% of the current world U production is accomplished preferentially by in situ recovery (ISR), 31,435 tons produced in 2019 (WNA, 2019), and does not produce equivalent tailings configurations. The radioactive descendants of U, representing 80% of the total initial radioactivity of the ore, are still present in the tailings (Abdelouas, 2006). Among these radionuclides, Ra-226 (half-life of 1600 years) is particularly studied because of its high specific activity (3.66 10^{10} Bq. g^{-1}) (Nirdosh et al., 1984; Molinari et al., 1990; Fesenko et al., 2014; Besançon et al., 2020) which leads to the continuous production of Rn-222 known for its radiotoxicity (Martin and Tuck, 1959; King et al., 1982). Most of the tailings are stored as piles close to the mining plants or disposed of by backfilling former uranium mines. Usually, once mining operations cease, tailings are protected by waste rocks or water cover, which form a radiological barrier against the emission of Rn-222, a radioactive gas descendant of Ra-226 (Robertson et al., 2019; Ballini et al., 2020; Chautard et al., 2020). The chemical and mechanical process of extracting uranium results in a reactive tailing environment containing residual and oxidized ores and chemical reagents such as sulfuric and nitric acid or lime, in the case of neutralization. In any case, the tailings evolve through a large variety of precipitation/dissolution processes controlling uranium migration.

The residual uranium found in the tailings comes from refractory uranium phases such as monazite (REE-$U^{IV}PO_4$) and brannerite (U^{IV}–Ti_2O_6) or from coffinite ($U^{IV}(SiO_4)_{1-x}$ $(OH)_{4x}$) and uraninite ($U^{IV}O_2$) when entrapped in quartz, feldspar, or mica, which inhibit their reactivity (Boekhout et al., 2015; Ballini et al., 2020; Chautard et al., 2020). However, if coffinite and uraninite grains are directly exposed to oxidizing conditions, these U(IV) minerals will oxidize with time into soluble uranyl groups ($[U^{VI}O_2]^{2+}$) that are known to be mobile (Grenthe et al., 2006). Under natural conditions, secondary minerals such as phyllosilicates, ferric oxyhydroxides or phosphates, generated by the weathering of primary rocks, control uranium migration through different processes, such as sorption or precipitation (Jin et al., 2016; Cretaz et al., 2013; Lee et al., 2011; Tayal et al., 2019; Lahrouch et al., 2021). In the tailings, secondary mineral neoformation depends on the nature of the ore parent rock, the chemical reagents used in the extraction or neutralization processes and the storage method. Therefore, gypsum and calcite formation are commonly observed in tailings due to the high concentrations of sulfates, calcium and carbonates related to the ore process (Jamieson, 2011; Lin et al., 2018). Uranyl ($UO_2{}^{2+}$) forms soluble complexes with a variety of anionic species, including sulfate, phosphate or carbonate, which tend to limit its hydrolysis and increase its mobility (Langmuir, 1978; Singh et al., 2010). The low solubility of uranyl phosphate complexes generally reduces uranium mobility. Conversely, sorption on mineral phases such as ferric oxyhydroxides or precipitation of secondary minerals such as uranyl phosphates tend to limit U mobility (His and Langmuir, 1985; Murakami et al., 1997).

Low pH and sulfate enrichment are commonly described in acid mine drainage (AMD) to favor the metal migration (Johnson and Hallberg, 2005; Morin and Calas, 2006; Park et al., 2019), including uranium (Evangelou et al., 1995; Edwards et al., 2000). Such an acidic rich sulfate environment is also reported in U-tailings, which are leached by sulfuric acid and not neutralized before their deposition (Carvalho et al., 2005; Déjeant et al., 2016). The sulfate groups form stable complexes with uranyl, whether in acidic conditions with the formation of binary uranyl sulfate complexes or at low to near-neutral pH conditions, which favor the formation of ternary uranyl hydroxosulfate complexes (Cox et al., 1989; Grenthe et al., 1992, 1993; Shock et al., 1997). Most uranyl sulfate complexes are soluble in dilute groundwaters and precipitate where evaporation is significant to form uranyl sulfate minerals (Finch and Murakami, 1999). Hence, the occurrence of uranyl sulfate minerals was observed under underground alteration conditions, both in weathering mining dumps (Krivovichev and Plàsil, 2013) and in mill-tailings (Schindler et al., 2012). Uranopilite formation, $(UO_2)_6SO_4O_2(OH)_6.(H_2O)_8$ occurs early in the alteration process of the primary U^{IV} phases involving acidic S-rich solution (Burns, 2001). This hydrated uranyl sulfate is easily hydrolyzed or dissolved and has a high U/S ratio. Moreover, uranopilite turns into meta-uranopilite after dehydration (Krivovichev and Plàsil, 2013). Zippeite group minerals are hydrated uranyl sulfates $M(UO_2)_4(SO_4)_2O_2(OH)_2.(H_2O)_4$, containing monovalent (K^+, Na^+, $NH_4{}^+$), divalent (Mg^{2+}, Zn^{2+}, Co^{2+}, Ni^{2+}, Cu^{2+}, Ca^{2+}), or trivalent (Y^{3+}, rare earth elements) cations. The zippeite structure was identified as uranyl sulfate sheets with cations located in the interlayer, such as Mg in octahedral coordination for magnesium zippeite (Brugger et al., 2003) or Na for natrozippeite (Sharifironizi and Burns, 2018).

Phosphates also play an important role in uranium migration. Indeed, like sulfates, phosphate groups form strong complexes with uranyl ions. The uranyl phosphate complexes can be sorbed on minerals such as ferrihydrite, which results in an increase in uranyl uptake on ferrihydrite (Payne et al., 1996; Lahrouch et al., 2021). The rather low solubility of these complexes leads to their precipitation as autunite or metatorbernite mineral groups (Cretaz et al., 2013). Under acidic conditions and depending on the ratio of carbonate to phosphate in the system, the solubility of uranyl phosphate complexes is lower than that of uranyl oxyhydroxides (Felmy et al., 2005; Grenthe and Konings, 1992; Langmuir, 1978; Rai et al., 2005). The formed uranyl phosphate minerals are relatively insensitive to the system redox potential and are also more resistant to dissolution than other uranium minerals, such as uraninite, under oxic conditions outside of their stability fields (Campbell et al., 2011; Sowder et al., 2001; Wellman, 2006; Wellman et al., 2009). Therefore, the precipitation of uranyl phosphates, dominated in the environmental systems by autunite and meta-autunite formation, prevents uranium mobility and holds uranium concentrations in groundwater rather low (Murakami et al., 1997, 2005; Jensen et al., 2002; Jerden et al., 2003; Denecke et al., 2005; Jerden and Sinha, 2003, 2006).

In the present study, we investigate the evolution of uranium-bearing phases in tailings from the COMINAK mine, Niger. Desert and subtropical weathering (Dodo and Zuppi, 1999) favor the formation of sulfate species through strong evaporation phenomena (Finch and Murakami, 1999). Previous results indicate local reconcentrations of U up to several thousand ppm within the tailings pile through oxidation and reprecipitation reactions associated with uranyl sulfate and phosphate occurrences (Déjeant et al., 2014, Déjeant et al., 2016; Angileri et al., 2018). In this paper, we present a thorough characterization of most U-enriched layers in the tailings pile, including both bulk and in situ characterizations. Extent X-ray Absorption to Fine Structure spectroscopy (EXAFS) and High Resolution X-Ray Diffraction (HR-XRD) were performed on powder samples to identify the dominant uranium species and parageneses. Space-resolved EXAFS spectroscopy and Wavelength Dispersive Spectroscopy (WDS) microprobe analyses on petrographic thin sections made it possible to identify neoformed uranyl sulfates and uranyl phosphates. Based on these valuable data, the occurrence of uranium-bearing phases related to the formation conditions as well as long-term uranium retention in the postmining environment will be discussed.

2. Materials and methods

2.1. Mining site description and associated sampling

The COMINAK mine opened in 1978 and produced approximately 2000 t U/year. The stratiform roll front-type deposit formed in lower Carboniferous Guezouman sandstones (quartz grains associated with feldspar and clay minerals). Most of the uranium occurrence is attributed to volcanic activity but to a lesser extent from erosion and leaching of the crystalline basement of the Aïr crystalline basement. Primary U-bearing phases are composed of micrometric uraninite and coffinite. Minor U refractory minerals are micrometric U–Ti and U–Mo oxides (Forbes, 1989; Pagel et al., 2005; Cavellec, 2006; Dejeant et al. 2014, 2016). The ore grade is approximately 4000 ppm but shows variation with time (~3000–5000 ppm). Ore processing is based on acidic and oxidizing dissolution. The ore is first crushed, then oxidized and leached with acid. This process liberates microphases of U associated with gangue and solubilizes U. The leaching operation is performed simultaneously with sulfuric acid and minor nitric acid. After flocculation using guar gum, the solid fraction (i.e., the mill tailings) is washed, and the U-rich pulp is filtered. The process efficiency is approximately 90–96%; thus, some residual U remains in the tailings after this step. Dissolved U is then stripped of the pregnant liquor using liquid solvents. U is finally recovered as MgU_2O_7 (s) (yellow cake). The tailings of COMINAK are not neutralized with lime and are therefore acidic. The pH of pore waters was determined to be less than 4.

This pile, containing approximately 22 million tons of tailings, is located in the Sahel Desert, where the climate is extremely arid with an annual mean temperature of 31 °C and annual precipitation of approximately 40 mm (Dodo and Zuppi, 1999). During deposition, fresh tailings are irrigated with mine water to reduce dust dispersion and improve the flow down the slopes of the pile. Strong evaporation phenomena occur, leading to the formation of a hardened crust (hard pan) at the surface of the pile.

Tailing samples containing high uranium concentrations were selected for this study (Déjeant et al., 2014, 2016). V126 and C11-14,5 were collected at the surface of the tailings pile and at 14.5 m depth in a former surface crust that has been buried over the years of activities (namely, paleolayer). Their uranium concentration is equal to 4100 ppm for V126 and 2250 ppm for C11-14,5, suggesting a strong U reconcentration.

2.2. Scanning electronic microscopy (SEM) and wavelength dispersive X-ray (WDS) spectroscopy microprobe

SEM images using backscattering electron mode (BSE) were recorded at 15, 20, and 25 keV on a ZEISS Supra 55 VP (ECCE TERRA, Observatoire des Sciences de l'Univers, Sorbonne University -INSU). WDS microprobe characterizations were achieved for Al, Ba, Ca, Fe, K, Mg, Mn, Mo, Na, P, S, Si, Th, Ti, V, Zr, Zn and U with a CAMECA SX-FIVE equipped with five WDS and one EDS detectors (CAMPARIS ECCE TERRA, Sorbonne University). The spatial resolution was set at 1 μm^2.

2.3. HR-XRD

Samples V126 and C11–14.5 were finely ground in an agate mortar for homogenization to prepare powder samples for X-ray diffraction (XRD) experiments. For each sample, approximately 20 mg was loaded into polyimide (Kapton) double capillaries (Microlumen, Oldsmar, USA) 0.5 mm in diameter. The XRD data were collected using a 2-circle diffractometer of the CRISTAL beamline at the SOLEIL synchrotron (Saint-Aubin, France) at λ 0.7270 Å, with an efficient Mythen 2 × 9K detector (Dectris, Switzerland) at 293 K. The goniometer was calibrated, and the wavelength was refined using the LaB_6 standard (NIST, SRM660a).

2.4. EXAFS measurements and data processing

XAFS experiments at the U L_{III} edge (E ($2p_{3/2}$) 17.166 keV) were performed at the INE-Beamline (Rothe et al., 2012) of the Karlsruhe Research Accelerator (KARA, Karlsruhe, Germany). The INE-Beamline is dedicated to the investigation of radionuclide materials with hard X-ray spectroscopy techniques. The EXAFS spectra were recorded on bulk samples conditioned as pellets with a diameter equal to 5 mm. The pellets were encapsulated by double-containment sample holders and cooled near 115 K using a LN_2 cryostat (Oxford Instruments OptistatDN) during data acquisition. Because of the low concentration of the samples, EXAFS measurements were performed in fluorescence yield detection mode averaging the U $L_{\alpha 1}$ fluorescence signal (~13.61 keV) recorded by a 4-element Vortex-ME4 SDD and a 1-element Vortex-60EX SDD (SIINT). The optics of the beamline comprises a double-crystal monochromator (DCM), fitted with a pair of Ge<422> crystals for selection of the required X-ray energy range, and a collimating and focusing mirror system (Rh-coated silicon mirrors), applied for higher-harmonic rejection, vertical collimation and focusing of the incident beam, respectively. The energy scale of the DCM was calibrated by assigning the first inflection point of the Y K-edge XANES (obtained from an yttrium metal foil measured in transmission mode) to the Y 1s-energy (17.038 keV). Spatially resolved EXAFS investigations were performed for petrographic thin section samples prepared by impregnation of sample aggregates in epoxy resin of 30 mm thickness glued on a glass substrate of 25 mm × 29 mm. Regions of interest were preselected from SEM images, showing high contrast for U rich aggregates. These regions were relocated by means of a visible light microscope aligned to the X-ray focus obtained by a polycapillary optic. A beam spot size of ~25 μm × 25 μm on the thin section samples was achieved. The U $L_{\alpha 1}$ fluorescence intensity was recorded by a 1-element Vortex-60EX SDD. Microfocus experiments were conducted at room temperature.

2.5. EXAFS data fitting

Data processing was conducted using the ATHENA code (Ravel and Newville, 2005). The e_o energy was identified at the maximum of the absorption edge for data fitting. Fourier transformation (FT) in k^2 was performed between 3 and 12 $Å^{-1}$ with Hanning windows using the ARTEMIS code (Ravel and Newville, 2005), except for the C11–14.5 thin section B sample, which is very noisy, and FT had to be performed between 3 and 8 $Å^{-1}$. Only one global amplitude factor $S_0{}^2$ and one energy threshold correction factor ΔE_0 were used in all paths. Phases and amplitudes were calculated using the FEFF6 simulation code (Rehr et al., 2010) included in ARTEMIS and based on the modified structure of menasite (Plášil et al., 2013), brannerite (Szymanski and Scott, 1982) and parsonsite (Locock et al., 2005) for uranyl sulfates, uranium oxide, and uranyl phosphate, respectively. In addition, a modified model of hydrogen uranyl phosphate tetrahydrate (Morosin, 1978), which has an equivalent structure to chernikovite or ankoleite, has been used for a uranyl phosphate mineral. Single scattering paths were considered for the oxygen, phosphorus, sulfur, iron or uranium atoms according to the sample. Triple Oax-U-Oax scattering paths were also considered and linked to the corresponding single paths for uranyl.

3. Results

3.1. Uranium speciation in bulk samples

XRD results with the diffractograms of V126 and C11–14.5 and the magnification of chosen angular domains of interest are shown in ESI Fig. 1 and Fig. 2 a to c, respectively. The two bulges at approximately 2.5 and 9.5 2θ on both diffractograms correspond to the Kapton tubes. Quartz, K and Na feldspars (orthoclase, microcline, albite) are detrital mineral heritages of the Akouta sandstone formation. Phyllosilicates are kaolinite, the main component, illite, smectite, interstratified chlorite/

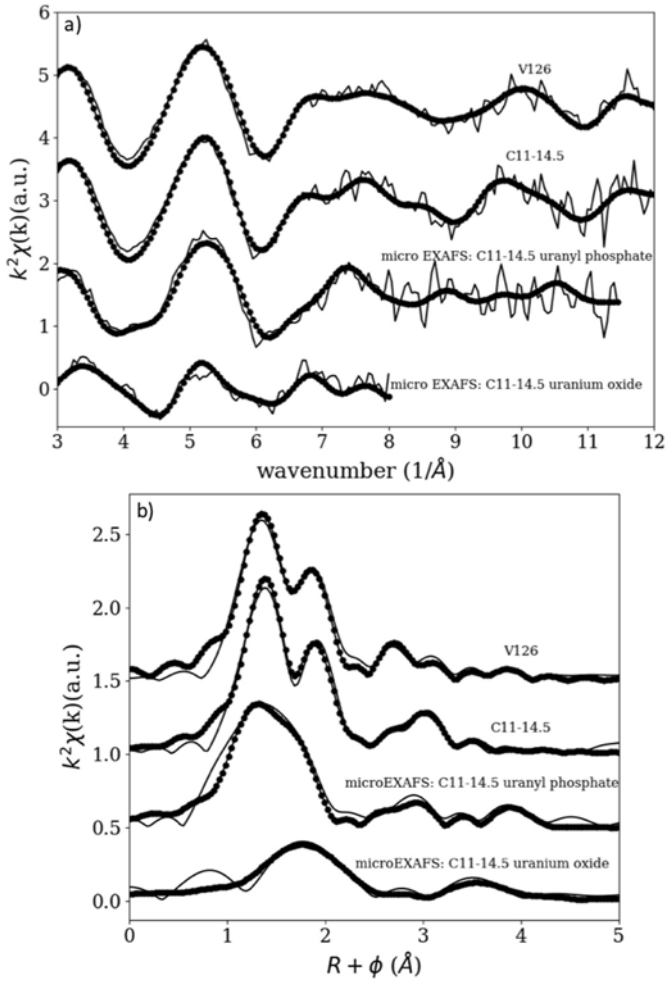

Fig. 1. a) EXAFS spectra of V126, C11–14.5 recorded on the bulk samples and micro EXAFS spectra recorded on uranyl phosphate rosettes and uranium oxide minerals found in C11–14.5. b) Corresponding FT of the EXAFS spectra. Solid line = experimental spectrum. Dotted line = adjustment. Spectra are shifted in ordinates for clarity.

smectite, and palygorskite. Like hematite/goethite, anatase, pyrite, and calcite, they are diagenetic signatures of sandstone formations. The only U(IV) primary phase of the initial ore is uraninite, identified in the surficial crust (V126) with peaks at 3.16 Å and 1.93 Å. Uranophane, mineral of the oxidized zone of the uranium deposit, is also identified in the surficial crust (V126) with peaks at 7.91, 3.95, 3.61, and 2.99 Å. These minerals were not identified in the paleolayer. Secondary minerals related to the U extraction process (sulfuric acid) in these two samples are sulfates such as gypsum, natro-jarosite, plumbo-jarosite, and jarosite. In the surficial crust sample, a higher variability of minerals is observed with peculiar minerals not identified in the paleolayer: hydrated minerals such as nordstrandite $Al(OH)_3$, todorokite $(Na,Ca,K)_2Mn_6O_{12}.3–4.5(H_2O)$, quenstedtite $Fe_2(SO_4)_3{\cdot}10(H_2O)$ and palygorskite $(Mg,Al)_2Si_4O_{10}(OH){\cdot}4(H_2O)$ but also anhydrite $(CaSO_4)$, witnesses of the evaporation conditions. In addition, diffraction peaks of apatite $(Ca_5(PO_4)_3(Cl/F/OH))$ are observed at 2.81 2.77 and 2.72 Å are observed in the surficial crust. In the C11–14.5 diffractogram, vivianite occurrence $(Fe^{2+}{}_3(PO_4)_2{\cdot}8H_2O)$ highlights different conditions of diagenesis in the paleolayer.

The experimental EXAFS spectra of V126 and C11–14.5 at the U L_{III} edge are shown in Fig. 1 a, and the corresponding FT is presented in Fig. 1 b. The FTs are not corrected for the EXAFS phase shift, so peaks appear at shorter distances (R+φ) than the true near-neighbor distances (R). The FT peaks below 1.5 Å are artifacts of spline removal and are not associated with any coordination distance. For each sample, the modulus of the FT exhibits the characteristic short-range axial shell of the two oxo bonds of $UO_2{}^{2+}$ for the first coordination sphere, of which the equatorial shell is also well resolved and indicates a single contribution. A second coordination sphere is visible between R+φ 2.2–3.3 Å with a weaker signal and a third between R+φ 3.3–4.2 Å for V126. The best fit metrical parameters are displayed in Table 1. For the two samples, the two axial oxygen atoms are located at 1.78 (1) Å. In the equatorial uranyl plane, the U-Oeq distances are found at 2.37 (1) Å for V126 and 2.41 (1) Å for C11–14.5. These distances are consistent with the number of equatorial oxygen atoms fixed to 5 (Burns, 2005). The Debye-Waller factor associated with the contribution of the equatorial oxygen atoms is rather high in both samples (σ^2 0.0081 Å^2 and σ^2 0.0091 Å^2 for V126 and C11–14.5, respectively), indicating disorder in the second coordination shell. This suggests that uranium is coordinated to small molecules such as H_2O, phosphates, or sulfates. The different types of equatorial oxygen atoms were not distinguished in the fits to limit the number of fitting parameters and because the k range was restricted to 3–12 Å^{-1}. A strong contribution near 3.56 Å is systematically observed, corresponding to Oax-U-Oax multiple scattering. The second coordination shell of uranium in V126 and C11–14.5 is composed of sulfur contributions located at 3.10 (2) Å and 3.17 (3) Å, respectively, corresponding to bidentate uranyl sulfates. The reported U···S distances for bidentate uranyl sulfates in the case of EXAFS experiments on soluble complexes of uranyl sulfates are approximately 3.12 Å (Moll et al., 2000; Hennig et al., 2008). This U···S distance can reach 3.17 Å in the case of quantum chemical calculations on various isomers of $UO_2(SO_4)$ and $UO_2(SO_4)_2{}^{2+}$ (Vallet and Grenthe, 2007). A second sulfur contribution at 3.62 (3) Å for V126 and at 3.63 (2) Å for C11–14.5 completes the second coordination shell of uranium. This U···S distance is consistent with those reported for monodentate uranyl sulfates (Moll et al., 2000; Hennig et al., 2008). The coordination numbers of bi and monodentate sulfates in V126, equal to 0.8 (2) and 0.8 (3), respectively, are lower than those in C11–14.5, equal to 2.1 (3) and 1.2 (2). This difference could be related to the higher hydration rate in the crust (V126), which is more impacted by hydration/evaporation cycles than the paleolayer (C11–14.5). The higher values of the Debye-Waller factor associated with the second coordination shell of uranium in C11–14.5 can also be explained by this difference in coordination numbers. An extra shell of uranium, composed of 0.4 (3) atoms at 3.94 (4) Å, is also needed to increase the fit quality of V126. The addition of the U–U contribution enhances the fit quality with an associated Rfactor and Qfactor equal to 1.3% and 5.34 respectively against 1.5% and 5.78 without the contribution. This weak uranium contribution could correspond to the formation of uranyl oxyhydroxides, but residual inherited uranophane, observed by HR-XRD, could not be excluded despite being a minor component.

3.2. Micromorphology , mineralogical and microgeochemical characterization of uranium phases in V126 and C11-14.5

Submicrometric mineralogical and chemical characterizations were performed on V126 and C11–14.5 prepared as petrographic thin sections. Uranium-bearing minerals were identified by SEM images (Fig. 2) combined with WDS microchemical analyses (Table 2) and mapping (Fig. 3 and ESI Fig. 3). To further clarify, the space-resolved chemical analyses, numbered one through thirteen, are marked by red crosses, and the WDS maps are marked by red squares. Each reported chemical composition is an average of five to ten measurements recorded around red crosses.

Inherited uranium phases from the initial ore were easily found in both the V126 and C11–14.5 samples, most having sizes less than 5 μm. Nanometric to micrometric uranium-titanium oxides are also dispersed in a chlorite/smectite matrix (Fig. 2a). Submicrometric crystal growth of uranium-titanium oxide on a montmorillonite pseudomorph occurred in fragmented quartz (Fig. 2b). These uranium-titanium oxides have

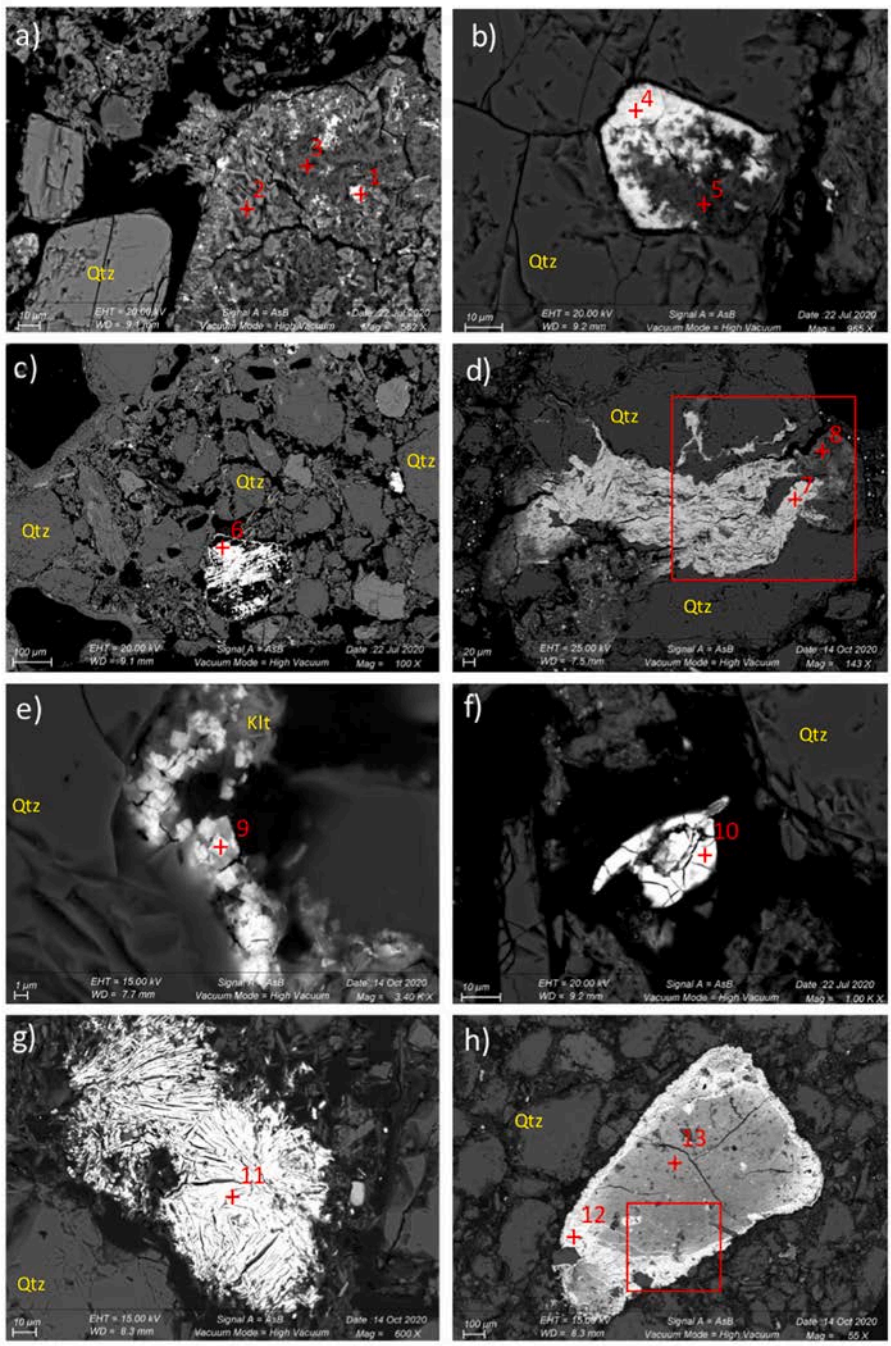

Fig. 2. Back-scattering electron pictures of U-bearing minerals observed in petrographic thin sections of the crust (V126) and paleolayer (C11–14.5). a) Uranium-titanium oxides dispersed in a chlorite/smectite matrix (V126). c) A concretion of uranium-molybdenate (V126). b) Uranium-titanium oxide on a montmorillonite pseudomorph occurred in fragmented quartz (Qtz) (V126). d) A large uranium-rich zone filling a quartz fissure (C11–14.5). e) Submicrometric cubic uranyl sulfate crystals growing on quartz within a kaolinite (Klt)-rich coating (V126). f) A uranyl sulfate mineral or concretion (V126). g) A crystalized uranyl phosphate (C11–14.5). h) A large uranyl phosphate coating on hydroxyapatite (C11–14.5). The 1–13 red crosses correspond to WDS analyses (Table 2), and the red squares mark the WDS maps. (For interpretation of the references to colour in this figure legend, the reader is referred to the Web version of this article.)

homogeneous chemical compositions, approximately 10 wt% Ti and ranging from 25.9 to 23.7 wt% U. (Table 2, areas 1 and 4). The related U/Ti ratios are equal to 2.49 and 2.30, respectively, which is close to the 2.48 found for brannerite (Willard et al., 1990). Iron (4.5 and 5.8 wt%), sulfur (1.8 and 2.8 wt%) and molybdenum (2.5 and 2.0 wt%) were also detected. Fe and S are common impurities in brannerite. The molybdenum is probably due to the presence of molybdenate relicts observed in both samples.

A large altered uranium-molybdenate (>100 μm), composed of 35.0 wt% uranium and 25.9% molybdenum, was observed in the V126 sample (Fig. 2c, Table 2, area 6). The related U/Mo ratio is equal to 1.35, a composition similar to moluranite, a hydrated U molybdenate found in the environment, with a U/Mo ratio of 1.41 (Willard et al., 1990). Moluranite is a common alteration product of brannerite that explains the ~2 wt % iron, sulfur and silicon concentrations detected.

In the paleolayer (C11–14.5), a large uranium-rich zone (>300 μm) filled a quartz fissure (Fig. 2d). The WDS map shows a heterogeneous distribution of uranium ranging from 10 wt% to 65 wt % (Fig. 3). The richest uranium areas are composed of uranium oxide aggregates of a few hundred nanometers (ESI Fig. 5). These nanometric uranium oxides (58.2 wt % mean uranium) occur in a smectite-rich matrix (Table 2, area 7, ESI Fig. 3). Impurities such as 2.5 wt % Ti, 1.6 wt % Fe and 1.3 wt % P are also measured in the fissure. Rutile dispersed in the fissure is observed. On the WDS maps, the iron and phosphorus concentrations display a differential distribution. The central part of the fissure exhibits low concentrations of iron and phosphorus (~2 wt % for both) and 60 wt % uranium. Conversely, higher concentrations of iron and phosphorus are detected in the extremities of the fissure (~10 wt % of Fe and ~7 wt

Table 1
EXAFS best-fit parameters for V126, C11–14.5 (bulk samples) and for the micro EXAFS analyses of uranyl phosphate rosettes and uranium oxide minerals found in C11-14. CNs were fixed to 2 for the axial and 5 for the equatorial oxygen atoms in the case of uranyl configuration (numbers in italics). The numbers in parentheses are the estimated uncertainties, σ^2 is the Debye-Waller factor of the scattering path, $S_0{}^2$ is the global amplitude factor, e0 is the energy threshold, R_{factor} is the quality factor of the fit in percent, and Q is the reduced $\chi_r{}^2$ factor of the fit.

	1st coordination shell	2nd coordination shell	Parameters
V126	*2* O_{ax} at 1.78 (1) Å σ^2 0.0026 Å^2	0.8 (2) S_{bid} at 3.10 (2) Å σ^2 0.0011 Å^2	$S_0{}^2$ 1.0 e_0 -0.35 eV
	5 O_{eq} at 2.37 (1) Å σ^2 0.0081 Å^2	0.8 (3) S_{mon} at 3.62 (3) Å σ^2 0.0015 Å^2	R_{factor} 1.3% Q 5.34
		0.4 (3) U at 3.94 (4) Å σ^2 0.0032 Å^2	
C11-14.5	*2* O_{ax} at 1.78 (1) Å σ^2 0.0021 Å^2	2.1 (3) S_{bid} at 3.17 (3) Å σ^2 0.0115 Å^2	$S_0{}^2$ 1.0 e_0 2.65 eV
	5 O_{eq} at 2.41 (1) Å σ^2 0.0091 Å^2	1.2 (2) S_{mon} at 3.63 (2) Å σ^2 0.0050 Å^2	R_{factor} 1.5% Q 1.39
C11-14.5 uranyl phosphate	*2* O_{ax} at 1.74 (1) Å σ^2 0.0059 Å^2	1.7 (7) P at 3.55 (3) Å σ^2 0.0111 Å^2	$S_0{}^2$ 1.0 e_0 1.48 eV
	5 O_{eq} at 2.25 (1) Å σ^2 0.0077 Å^2	1.4 (5) U at 4.02 (3) Å σ^2 0.0062 Å^2	R_{factor} 2.0% Q 2.08
C11-14.5 uranium oxide	7.2 (4) O at 2.37 (1) Å σ^2 0.0240 Å^2	2.7 (5) U at 3.85 (2) Å σ^2 0.0067 Å^2	$S_0{}^2$ 1.0 e_0 2.10 eV
	1.7 (3) O at 2.83 (2) Å σ^2 0.0045 Å^2		R_{factor} 2.5% Q 3.71

% of P) and 10 wt % of uranium, suggesting a local alteration/dissolution process of these inherited uranium oxides (Table 2, area 8).

Submicrometric cubic uranyl sulfate crystals growing on quartz within a kaolinite-rich coating were identified in the crust (V126) (Fig. 2e). Microprobe analyses provide evidence of iron sulfide as well in a background. A larger uranyl sulfate mineral or concretion of a few tens of micrometers was also observed in this sample (Fig. 2f). The crystal composition is 23.1 wt % U and 4.4 wt % S (Table 2, area 9). The uranium concentration of the micrometric uranyl sulfate mineral is higher than that of the small crystals (49.1 wt %), and the sulfur rate is equivalent (Table 2, area 10). The U/S ratio of the crystals is equal to 5.25, whereas it is equal to 10.9 for the mineral. The different micromorphologies and sizes suggest the formation of two different phases of uranyl sulfates. The various sulfate neoformations in both the surficial crust and paleolayer are related to extraction processes based on sulfuric acid leaching.

Uranyl phosphates from a few tens to a few hundreds of micrometers were only found in the paleolayer (Fig. 2 g and h). With a fan and sheet structure in the porosity of the tailings, they are composed of 53.1 wt % uranium and 6.4 wt % phosphorus (Table 2, area 11). A large uranyl phosphate coating (over 100 μm) with the same sheet structure and chemical composition was also identified on a hydroxyapatite aggregate (Fig. 2 h, ESI Fig. 4). The high concentrations of phosphorus and calcium detected on the aggregate, 14.7 and 31.3 wt %, respectively (Table 2, area 13), correspond to hydroxyapatite composition. The U/P ratio is similar to the 7.6 value of uranyl phosphates, such as chernikovite or lermontovite. The highest uranium concentration (55 wt%) occurs in the coating and fissure infillings of hydroxyapatite. It should be noted that approximately 6 wt % uranium is detected in the richest hydroxyapatite and central part of the aggregate. This value may be attributed to dispersed submicrometric crystals of uranyl phosphates and eventually uranium sorption on hydroxyapatite (Fuller et al., 2002). According to their occurrence, micromorphology and sizes, these uranyl phosphate minerals are considered newly formed.

3.3. μEXAFS characterizations of U-bearing minerals in C11–14.5

EXAFS characterizations of both uranium oxide located in the crack, fissures (Fig. 2d) and uranyl phosphate coating growing on hydroxyapatite (Fig. 2 h) were performed at the U L_{III} edge using a beam of 25 μm × 25 μm. These two minerals are located in the paleolayer (C11–14.5). The sample was prepared as a petrographic thin section that allowed us to precisely probe uranium speciation in these two minerals. The recorded EXAFS spectra are shown in Fig. 1a, and the corresponding FT is presented in Fig. 1b. Despite an extended acquisition time between 1 and 13 k and the merging of eight spectra, noise is important in these two EXAFS spectra and forces us to fit until 11.5 k for uranyl phosphate and 8 k for uranium oxide. The best fit metrical parameters are displayed in Table 1.

For uranium oxide, the modulus of the FT exhibits two strong contributions visible at R+φ 1.5–2.5 Å and R+φ 3.1–4 Å, corresponding to the first and second coordination shells of uranium (Fig. 1b). The shape and the R+φ of the first contribution confirm a U(IV) mineral. The coordination shell of uranium is composed of 7.2 (4) oxygen atoms at 2.37 (1) Å and 2.5 (5) uranium atoms at 3.85 (2) Å, which is consistent with the U–O and U–U distances reported for uraninite (Kelly, 2010). The weak contribution visible at R+φ 2.5–3 Å can be fitted with a U–O distance of 2.83 (2) Å, but this value is too long to be physically reasonable for a uranium-oxygen bond length. The scattering contribution of this shell is assumed to be mainly a contribution of silicon related to the mineral background of the fissure composed of kaolinite. The coffinite $USiO_4$ contains a similar U–Si contribution reported to be 3.09 Å for the SiO_4 polyhedron coordinated in a bidentate, edge-sharing fashion (Dreissig et al., 2011; Fuchs and Gebert, 1958). The low Si concentration detected by WDS in this area (2.2 wt%, Table 2, area 7) is not consistent with the Si concentration in coffinite (~7 wt%), which excluded the possibility of coffinite occurrence (Willard et al., 1990).

Despite its low resolution, the FT modulus of uranyl phosphate (Fig. 1b) exhibits the short-range axial shell of the two oxo bonds of $UO_2{}^{2+}$. A shoulder associated with the first contribution is also visible corresponding to the equatorial shell. The second and third coordination spheres have a weaker signal and are located at R+φ 2.2–3.3 Å and R+φ 3.5–4.1 Å, respectively. The first coordination shell is composed of two axial and five equatorial oxygen atoms at 1.74 (1) Å and 2.25 (1) Å, respectively. A total of 1.7 (7) phosphorus atoms at 3.55 (3) Å from monodentate phosphate groups form the second coordination shell (Vazquez et al., 2007; Kelly, 2010). The third coordination shell composed of 1.4 (5) uranium atoms at 4.02 (3) completes the coordination shell of uranium. The U-Oeq and U–P distances were close to those reported for meta-autunite ($Ca(UO_2)_2(PO_4)_2{\cdot}6H_2O$) and meta ankoleite ($K_2(UO_2)_2(PO_4)_2{\cdot}6H_2O$) (Thompson et al., 1997) but no calcium or potassium were detected by WDS (Table 2). The identification of the uranyl phosphate phase based only on the EXAFS data is difficult. Nevertheless, the reported U–P and U–U distances are similar to those reported for uranyl orthophosphate (Catalano et al., 2004) and the presence of hydroxyapatite could support the formation of uranyl orthophosphate (Locock et al., 2002). A multiple scattering contribution, Oax-U-Oax, near 3.56 Å is also needed to fit the experimental data. Together, the EXAFS and WDS results confirm the occurrence of uranyl phosphate in the paleolayer.

4. Discussion

4.1. Uranium speciation and paragenese

EXAFS spectroscopy, HR-XRD, micromorphology, mineralogical and

Table 2
WDS microchemical analyses recorded on V126 and C11–14.5 thin sections. Each reported chemical composition (in wt %) is an average of five to ten measurements except for 2, 3 and 5. The values are presented with their standard deviations. The probed area (1 μm × 1μm) is identified by red crosses (Fig. 2), numbered one through thirteen.

	Al	Si	K	Ca	Na	Fe	S	P	Mo	Ti	U	O*	total
1	2.71	7.88	0.31	0.51	0.47	5.84	2.76	0.79	2.04	10.32	23.72	30.39	92.35
	±	±	±	±	±	±	±	±	±	±	±	±	±
	0.38	1.73	0.11	0.08	0.13	2.11	0.23	0.09	0.21	1.05	3.48	1.38	0.73
2	15.96	25.32	7.00	0.14	0.18	2.23	0.56	0.15	0.00	0.05	0.13	47.38	101.59
	±	±	±	±	±	±	±	±	±	±	±	±	±
	nc	nc	nc	nc	nc	nc	nc	nc	nc	nc	nc	nc	nc
3	15.13	21.67	0.24	0.21	0.11	2.51	1.21	0.27	0.25	0.45	0.34	43.84	90.80
	±	±	±	±	±	±	±	±	±	±	±	±	±
	nc	nc	nc	nc	nc	nc	nc	nc	nc	nc	nc	nc	nc
4	2.57	4.89	0.28	0.34	0.21	4.49	1.80	0.53	2.49	10.44	25.95	24.95	82.04
	±	±	±	±	±	±	±	±	±	±	±	±	±
	0.52	1.73	0.31	0.13	0.06	0.14	0.52	0.03	0.22	0.25	1.22	2.49	4.18
5	9.56	20.92	0.86	0.07	0.17	2.18	2.84	0.27	0.51	0.85	2.02	38.76	81.26
	±	±	±	±	±	±	±	±	±	±	±	±	±
	nc	nc	nc	nc	nc	nc	nc	nc	nc	nc	nc	nc	nc
6	0.42	2.59	0.00	0.00	0.16	1.89	1.68	0.18	25.93	0.15	35.02	23.31	91.01
	±	±	±	±	±	±	±	±	±	±	±	±	±
	0.42	0.85	0.08	0.07	0.06	1.38	0.21	0.03	2.00	0.04	3.50	1.80	6.42
7	1.24	2.18	0.35	1.36	0.31	1.60	0.11	1.30	0.68	2.51	58.15	17.49	90.36
	±	±	±	±	±	±	±	±	±	±	±	±	±
	0.38	0.66	0.31	0.18	0.03	0.03	0.02	0.18	0.01	0.05	2.82	1.04	0.15
8	8.04	14.41	2.84	0.52	0.27	6.3	0.24	4.50	0.79	1.73	4.92	36.74	86.72
	±	±	±	±	±	±	±	±	±	±	±	±	±
	1.84	3.50	0.55	0.07	0.09	1.53	0.09	2.01	0.29	0.76	1.13	1.98	3.17
9	5.22	5.29	0.32	0.18	0.31	1.74	4.43	0.47	0.05	0.04	23.07	20.09	61.69
	±	±	±	±	±	±	±	±	±	±	±	±	±
	3.50	3.75	0.31	0.01	0.05	0.27	0.92	0.11	0.08	0.03	0.90	7.15	16.27
10	0.25	0.27	0.00	0.10	0.10	0.21	4.54	0.05	0.00	0.02	49.12	13.35	70.61
	±	±	±	±	±	±	±	±	±	±	±	±	±
	0.35	0.18	0.04	0.17	0.06	0.09	0.72	0.04	0.13	0.05	5.22	1.30	6.58
11	0.09	0.25	0.05	0.34	0.09	1.87	0.14	6.42	0.00	0.17	53.08	17.29	81.34
	±	±	±	±	±	±	±	±	±	±	±	±	±
	0.04	0.16	0.09	0.21	0.04	0.99	0.14	0.61	0.08	0.06	4.31	1.07	5.40
12	0.51	0.95	0.21	0.27	0.07	2.05	0.13	7.54	0.17	0.07	54.56	20.48	89.25
	±	±	±	±	±	±	±	±	±	±	±	±	±
	0.46	0.74	0.10	0.06	0.02	0.51	0.09	0.37	0.22	0.04	1.03	1.13	1.66
13	1.51	1.84	0.70	27.50	0.21	1.69	1.20	14.39	2.32	0.29	7.17	37.69	96.69
	±	±	±	±	±	±	±	±	±	±	±	±	±
	0.24	0.64	0.21	3.43	0.25	0.95	0.85	0.53	2.39	0.23	1.23	2.64	6.67

microgeochemical characterization procedures were combined in this study to determine the mechanisms ruling uranium mobility in the Cominak tailing pile. The selected samples V126 and C11–14.5 were collected in the surficial crust and in a paleolayer (C11–14.5), a former surficial crust located at 14.5 m depth, of the pile. The high U concentrations of these two environmental samples, 4100 ppm for V126 and 2250 ppm for C11-14,5, suggest a strong U reconcentration. EXAFS spectroscopy performed on the bulk samples provided valuable data about dominant U speciation in the samples. HR-XRD allowed us to describe the paragenesis and identify uranium-bearing minerals. Micromorphology, microgeochemical analyses, and micro-EXAFS spectroscopy performed on petrographic thin sections of the samples made possible the characterizations of specific uranium phases, inherited or newly formed, and highlighted mechanisms ruling the uranium immobilization.

The formation of uranyl (U^{VI}) groups was detected in the U-tailings samples by EXAFS spectroscopy. In both samples, uranyl is mainly associated with sulfate groups (Table 1), which is consistent with the chemical and environmental conditions occurring in the U-tailings pile of Cominak. This pile is ruled by acidic pH and anthropic sulfur rich environments. Oxidizing conditions and strong evaporation phenomena related to the extremely arid Sahelian climate induce the neoformation of uranyl sulfates (Finch and Murakami, 1999). Various sulfate species were detected by HR-XRD in the samples, such as gypsum $CaSO_4$. $2H_2O$, natrojarosite $NaFe_3(SO4)_2(OH)_6$, plumbojarosite $PbFe_3(SO_4)_2(OH)_6$ and quenstedtite $Fe_2(SO_4)_3{\cdot}11H_2O$. Sulfur contributions were identified in the coordination shell of uranyl at 3.10 Å and 3.17 Å as well as 3.62 Å corresponding to bi and monodentate uranyl sulfates (Moll et al., 2000; Vallet and Grenthe, 2007; Hennig et al., 2008).

Indications regarding the hydration rate can be deduced from the coordination numbers, equal to 0.8 for bidentate and monodentate sulfur atoms in the surficial crust, while there are equal to 2.1 and 1.2 for bidentate and monodentate sulfur atoms in the paleolayer. Among the five oxygen atoms composing the equatorial shell of V126, 1.6 come from bidentate sulfates (2x0.8) and 0.8 come from monodentate sulfates. The 2.6 remaining oxygen atoms correspond to water molecules. In C11–14.5, the oxygen equatorial shell is composed of 4.2 O from bidentate sulfates (2x2.1) and 1.2 from monodentate sulfates which confirm the absence of water molecule in the coordination shell. Following this method, the equatorial shell would be composed of 5.4 oxygen atoms. According to the estimated uncertainties, this value is consistent with the value of this parameter in the fit fixed to 5. The average distance of the oxygen equatorial shell also brings information about the composition of the coordination shell. Considering the average distances of uranium-oxygen from monodentate sulfate (2.30–2,37 Å), bidentate sulfate (2.42–2.48 Å) and waters molecules (2.41 Å) (Hennig et al., 2007), it is possible to calculate theoretical distances of the oxygen equatorial shell. For V126 this theoretical distance is equal to 2.41 Å ((2.33 × 0.8 O_{Sbid} + 2.45x1.6 O_{Smon} + 2.41x2.6O_{water})/5 2.41) and for C11–14.5 to 2.42 Å ((2.33 × 1.2 O_{Sbid}

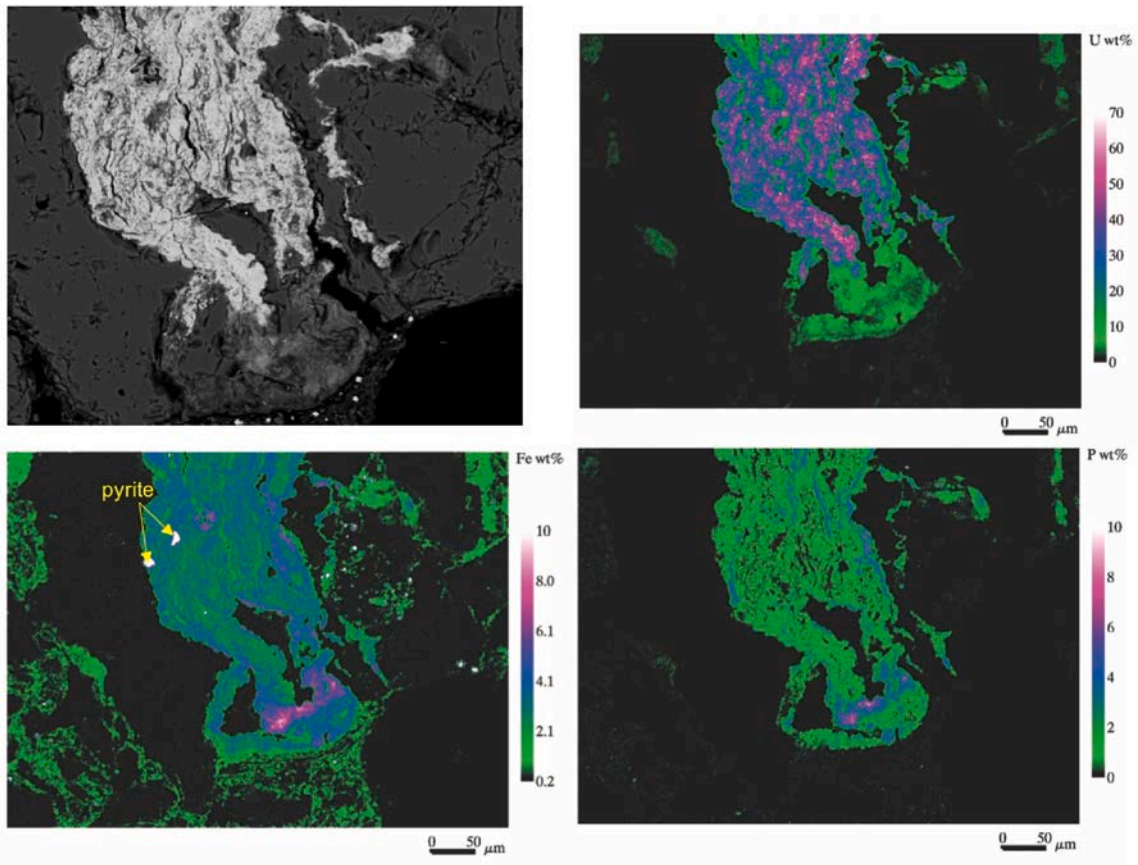

Fig. 3. Back-scattering electron map of a portion of the C11–14.5 petrographic thin section with uranium oxides in a quartz fissure. Corresponding wavelength dispersive X-ray maps of uranium, iron and phosphorus. The scale is calculated in elementary mass percent (wt%). The white pixels correspond to the highest concentration, and the black pixels indicate the lowest. The pixel size is 1 µm × 1 µm.

+ 2.45x4.2 O_{Smon})/5.4) 2.42). For C11–14.5 the result is consistent with the EXAFS data but for V126 the result is higher of 0.04 Å. The presence of oxygen atoms from clay minerals in the coordination shell of the uranyl, in addition to those from water molecules, could explain this difference and indicate minor sorption phenomena on clay minerals. The higher hydration rate of the surficial crust sample is related to the Sahelian climate. Minerals such as norstrandite in the surficial sample and anhydrite confirm the variability of hydrometric occurrence at the surface. The paleolayer located at 14.5 m depth is protected from surficial meteoric conditions with more constant hydrometric conditions.

Uranyl sulfate minerals were only identified as micrometric cubic minerals or as microconcretion in the surficial crust by SEM and WDS microprobe in petrographic thin sections (Fig. 2e and f). They were not detected in the HR-XRD diffractograms. The neoformation of uranyl sulfate minerals is therefore considered to be a minor process compared to the formation of soluble forms of uranyl sulfate. The higher coordination number associated with the sulfate groups in the paleolayer suggests the neoformation of uranyl sulfate minerals. However, it was not observed in the paleolayer sample by SEM and WDS microprobes.

In the surficial crust, relict primary uranium minerals were identified. Uranophane was detected by HR-XRD as well as minor occurrence of uraninite (ESI Fig 2abc). Uranophane, the U(VI) mineral resulting from the supergene alteration of uraninite, is more resistant to the extraction process. Despite the high efficiency of the U-extraction process (95–98%), uraninites resist the extraction process, especially when trapped in minerals such as quartz, feldspar, or mica. A weak U–U contribution at 3.94 Å was identified by EXAFS spectroscopy (Table 1). This U–U contribution is attributed to the formation of uranyl oxides certainly formed from the oxidation of relict uranium primary minerals. Although a U–U contribution at 3.94 Å was reported for uranophane (Catalano et al., 2004; Kelly, 2010), this U mineral is a minor component of the V126 sample. Uranophane is rarely observed in tailings, and its detection is related to the high sensitivity of HR-XRD for minor phases. In the bulk sample of the paleolayer, no inherited uranium minerals were detected by EXAFS or HR-XRD, related to the detection limits. Compared to the surficial layer, it suggests a reduced occurrence of these minerals, probably due to time-related dissolutions according to the oxidizing conditions in the pile.

Micromorphological in situ observations on petrographic thin sections highlight other residual uranium phases in both samples, possibly minor for some of them. Submicrometric crystals of brannerite, ((U,Ca, Ce) $(Ti,Fe)_2O_6$), are dispersed in a chlorite/smectite matrix aggregate with relicts of K felspars (Fig. 2a) but also as nanometric spherules associated with montmorillonite neoformations entrapped in a quartz crystal (Fig. 2b). These oxides are refractory uranium minerals of the ore and resist the U-extraction process (Lottering et al., 2008; Charalambous et al., 2014). The clay minerals result from supergene alteration prior to the extraction process. A uranium-molybdenum oxide such as moluranite was also observed in the V126 sample in a millimetric aggregate of quartz feldspar clay minerals with dispersed micrometric pyrites, zircons, and galenas (Fig. 2c). Moluranite, a U(IV)/U(VI) amorphous alteration product of brannerite, formed when brannerite was highly altered by the extraction process.

A large U-rich zone located in a quartz fissure was identified in the paleolayer (Fig. 2d). U concentration is approximately 58 wt%. Uranium (IV) was detected by space-resolved EXAFS spectroscopy on a petrographic thin section. The number of uranium next neighbors equal to 2.5 is too low to be crystalline uraninite, which has 12 uranium next neighbors (Conradson et al., 2004; Catalano and Brown, 2004). The low coordination number is a result of a strong structural disorder possibly

related to the nanometric size of the uranium (IV) oxide aggregates (ESI Fig. 5). A weak single scattering contribution at 2.83 (2) Å is attributed to silicon atoms related to the smectite infilling observed in the fissure (ESI Fig. 3). This Si contribution was described by Dreissig et al. during the formation of U(IV) colloids in the presence of aqueous silicate solution (Dreissig et al., 2011). The U(IV) oxide and smectite overgrowths in such fissures of quartz suggest inherited phases of supergene alteration prior to the U-extraction process.

A heterogeneous distribution of uranium is observed in the fissure (Fig. 3) with U-concentrations ranging from 35 wt% to 65 wt%, related to the growth of uranium (IV) spherules on the smectite sheets in the closed part of the fissure. When no uranium (IV) spherules are visible in the fissure, the smectite is 5 wt% U enriched. It could be attributed to U sorption. In the open part of the fissure, the U concentration is approximately 10 wt%, suggesting alteration of the uranium (IV) oxide concretions. In this zone affected by alteration fluids, the mean concentrations of iron and phosphorus are 7 and 5 wt %, respectively. The formation of iron oxides and phosphate groups refers to recent alteration conditions and postextraction processes (Lahrouch et al., 2021). The colocalization of Fe and P observed on the WDS map highlights a combination of iron oxide with phosphate groups that forms a trap for uranium. This mechanism of uranium immobilization was already observed and described in U-waste rock piles submitted to weathering (Lahrouch et al., 2021). In this open area feature, the smectitic background is also another complementary trap of U immobilization.

Uranyl phosphate minerals were observed in the paleolayer as a few hundred micrometers rosettes in the porosity of the samples (Fig. 2 g) or as coatings on hydroxyapatite (Fig. 2 h). They are composed of ~55 wt % uranium and 7 wt % phosphorus (Table 2, area 7). The uranyl coordination shell composed of monodentate phosphate groups and uranium is consistent with the formation of uranyl orthophosphate (Catalano et al., 2004; Locock and Burns, 2002). The uranyl groups are immobilized by uranyl phosphate mineral neoformations known as insoluble phases. The P source for phosphates is the accessory mineral apatite observed by SEM/WDS. Uranyl phosphate coatings on hydroxyapatite aggregates confirm the local dissolution and reprecipitation of P. These uranyl orthophosphates may result from the dissolution of apatite under acidic conditions controlled by Ca liberation (Dorozkhin, 1997). These strong acidic conditions explain why more common autunite neoformations were not observed (Kelly, 2010). Apatite is observed in the XR diffractogram of the surficial crust but not in that of the paleolayer. This suggests a weak occurrence of this mineral in the paleolayer and confirms the in situ alteration/transformation of apatite in uranyl orthophosphate. Another phosphate mineral, vivianite, a ferrous phosphate, suggests variable local redox conditions, which is consistent with the conservation of relicts of uraninite in the global oxidized facies.

The tailings pile is a hydrated sulfate-rich environment with gypsum, jarosite, and quenstedtite (less than 2 wt% S). As described by EXAFS, uranyl is mainly associated with sulfate groups, which are relative traps for uranium. Rare uranyl sulfate minerals were observed by SEM/WDS, suggesting that neoformation is not the dominant process. The surficial crust is submitted to cyclic evapotranspiration conditions of the Sahelian climate. Local anhydrite occurrence in the surficial crust attests to a more arid period. These peaks of evaporation favor the precipitation of uranyl sulfate minerals. In the paleolayer, the conditions of hydration and temperature are more stable than in the surface. The uranyl groups are associated with sulfate complexes, and the sulfate parageneses are similar to those in the surficial crust except for quenstedtite. The neoformation of uranyl phosphate minerals competes with uranyl sulfate minerals. The uranyl phosphate minerals precipitate according to solubility constants (Gorman-Lewis et al., 2008) and possible pH modification. The P source for these phosphate neoformations is the accessory mineral apatite from the Guezouman sandstone, which also occurs in the surficial layer. The paleolayer, which is an ancient U-rich surface of the tailings, evolves with time and confined medium to a globally more stable environment for uranyl immobilization. Local reduced phases such as uraninite and vivianite endure, but if redox conditions evolve, the vivianite alteration will possibly act as another trap.

5. Conclusions

Uranium mobility in the two major U-enriched layers of the tailings pile of COMINAK was studied at micrometric and molecular scales, the surficial crust and the 14.5 m deep paleolayer (an ancient surficial hard pan). The tailings were not neutralized with lime after the sulfuric acidic U extraction process. Acidic conditions control the uranyl speciation in the pile. Uranyl is mainly associated with the sulfate groups. Neoformation of uranyl sulfates is favored by strong evapotranspiration phenomena due to Sahelian climates.

Uranyl phosphate occurrence in the deep paleolayer protected from surficial climatic conditions, suggesting that more stable hydration states and temperatures are efficient traps for uranium long-term mobility. The main source of P is apatite from the Guezouman sandstone dispersed in the tailings. In the paleolayer, local reduced conditions perdure with uraninite and vivianite occurrence. This other P source will possibly control the long-term mobility of uranium in case of modification of the redox conditions.

Credit author statement

Florian Lahrouch made the EXAFS, HR-XRD and WDS studies + wrote the manuscript. Benoit Baptiste manages the BAG program to perform HR-XRD characterizations on CRISTAL Beamline and helped to the HR-XRD data recording. Kathy Dardenne and Jorg Rothe are the INE beamline Scientists who helped to the EXAFS data recording. Erik Elkaim is the CRISTAL beamline Scientists who helped to the HR-XRD data recording. Michael Descostes supplied the samples, and brought his knowledge of post mining environment. Martine Gerard made the EXAFS, HR-XRD and WDS studies + wrote the manuscript.

Declaration of competing interest

The authors declare that they have no known competing financial interests or personal relationships that could have appeared to influence the work reported in this paper.

Acknowledgments

The authors acknowledge the KIT light source for provision of beamtime at the INE-Beamline operated by the Institute for Nuclear Waste Disposal and would like to thank the Institute for Beam Physics and Technology (IBPT) for the operation of the storage ring, the Karlsruhe Research Accelerator (KARA).

In the framework of the CNRS ЯÉCIPROCS network, this work has been accepted for synchrotron beamtime by the Soleil scientific proposal committee (BAG proposals 20191509). The authors would like to thank the SOLEIL Synchrotron Facility for use of radiation facilities.

The authors also sincerely thank Omar Boudouma (Plateforme MEB-OSU, Sorbonne Université) for acquisition of SEM images and Michel Fialin and Nicolas Rividi (CAMPARIS, Sorbonne Université) for wavelength-dispersive spectroscopy (WDS) measurements.

The authors thank ORANO Mining and COMINAK staff for their access to the samples. This work was supported by ORANO Mining, Environmental R&D Department.

References

Abdelouas, A., 2006. Uranium mill tailings: geochemistry, mineralogy, and environmental impact. Elements 2, 335–341.

Angileri, A., Sardini, P., Donnard, J., Duval, S., Lefeuvre, H., Oger, T., Patrier, P., Rividi, N., Siitari-Kauppi, M., Toubon, H., Descostes, M., 2018. Mapping 238U decay chain disequilibrium state in thin sections of geomaterials by digital autoradiography and microprobe analysis. Appl. Radiat. Isot. 140, 228–237.

Ballini, M., Chautard, C., Nos, J., Phrommavanh, V., Beaucaire, C., Besançon, C., Boizard, A., Cathelineau, M., Peiffert, C., Vercouter, T., Vors, E., Descostes, M., 2020. A multi-scalar study of the long-term reactivity of uranium mill tailings from Bellezane site (France). J. Environ. Radioact. 106223.

Besançon, C., Chautard, C., Beaucaire, C., Savoye, S., Sardini, P., Gérard, M., Descostes, M., 2020. The role of barite in the post-mining stabilization of radium-226: a modeling contribution for sequential extractions. Minerals 10, 497.

Boekhout, F., Gérard, M., Kanzari, A., Michel, A., Déjeant, A., Galoisy, L., Calas, G., Descostes, M., 2015. Uranium migration and retention during weathering of granitic waste rock piles. Appl. Geochem. 58, 123–135.

Brugger, J., Burns, P.C., Meisser, N., 2003. Contribution to the mineralogy of acid drainage of Uranium minerals: marecottite and the zippeite-group. Am. Mineral. 88, 676–685.

Burns, P.C., 2001. A new uranyl sulfate chain in the structure of uranopilite. Can. Mineral. 39, 1139–1146.

Burns C, P, 2005. U6+ minerals and inorganic compounds: insights into an expanded structural hierarchy of crystal structures. Can. Mineral. 1839–1894.

Campbell, K.M., Veeramani, H., Ulrich, K.-U., Blue, L.Y., Giammar, D.E., Bernier-Latmani, R., Stubbs, J.E., Suvorova, E., Yabusaki, S., Lezama-Pacheco, J.S., Mehta, A., Long, P.E., Bargar, J.R., 2011. Oxidative dissolution of biogenic uraninite in groundwater at Old Rifle, CO. Environ. Sci. Technol. 45, 8748–8754.

Carvalho, I.G., Cidu, R., Fanfani, L., Pitsch, H., Beaucaire, C., Zuddas, P., 2005. Environ. Sci. Technol. 39, 8646–8652.

Catalano, J.G., Brown Jr., G.E., 2004. Analysis of uranyl-bearing phases by EXAFS spectroscopy: interferences, multiple scattering, accuracy of structural parameters, and spectral differences. Am. Mineral. 89, 1004–1021.

Cavellec, S., 2006. Evolution diagénétique du bassin de Tim Mersoï et conséquences pour la genèse des minéralisations uranifères dans les formations carbonifères du Guezouman et du Tarat (district Arlit-Akokan, Niger). Université Paris XI.

Charalambous, F.A., Ram, R., McMaster, S., Pownceby, M.I., Tardio, J., Bhargava, S.K., 2014. Leaching behaviour of natural and heat-treated brannerite-containing uranium ores in sulphate solutions with iron(III). Miner. Eng. 57, 25-35.

Chautard, C., Beaucaire, C., Gerard, M., Roy, R., Savoye, S., Descostes, M., 2020. Geochemical characterization of uranium mill tailings (Bois Noirs Limouzat, France) highlighting the U and 226Ra retention. J. Environ. Radioact. 218, 106251.

Conradson D, S, Manara, D, Wastin, F, Clark L, D, Lander H, G, Morales A, L, Rebizant, J, Rondinella V, V, 2004. Local structure and charge distribution in the UO2−U4O9 system. Inrog. Chem. 43, 6922–6934.

Cox, J.D., Wagman, D.D., Medvedev, V.A., 1989. Codata Key Values for Thermodynamics. Hemisphere Publications, New York.

Cretaz, F., Szenknect, S., Clavier, N., Vitorge, P., Mesbah, A., Descostes, M., Poinssot, C., Dacheux, N., 2013. Solubility properties of synthetic and natural meta-torbernite. J. Nucl. Mater. 442, 195–207.

Déjeant, A., Bourva, L., Sia, R., Galoisy, L., Calas, G., Phrommavanh, V., Descostes, M., 2014. Field analyses of ^{238}U and ^{226}Ra in two uranium mill tailings piles from Niger using portable HPGe detector. J. Environ. Radioact. 137, 105–112.

Déjeant, A., Galoisy, L., Roy, R., Calas, G., Boekhout, F., Phrommavanh, V., Descostes, M., 2016. Evolution of uranium distribution and speciation in mill tailings, COMINAK Mine, Niger. Sci. Total Environ. 545–546, 340–352.

Denecke, M.A., Janssens, K., Proost, K., Rothe, J., Noseck, U., 2005. Confocal micrometer-scale X-ray fluorescence and X-ray absorption fine structure studies of uranium speciation in a tertiary sediment from a waste disposal natural analogue site. Environ. Sci. Technol. 39, 2049–2058.

Dodo, A., Zuppi, G.M., 1999. Variabilité climatique durant le Quaternaire dans la nappe du Tarat (Arlit, Niger). C.R. Acad. Sci. Ser. IIA Earth Planet. Sci. 328, 371–379.

Dorozhkin, S.V., 1997. Surface reactions of apatite dissolution. J. Colloid Interface Sci. 191, 489–497.

Dreissig, I., Weiss, S., Hennig, C., Bernhard, G., Zanker, H., 2011. Formation of uranium (IV)-silica colloids at near-neutral pH. Geochem. Cosmochim. Acta 75, 352–367.

Edwards, K.J., Bond, P.L., Druschel, G.K., McGuire, M.M., Hamers, R.J., Banfield, J.F., 2000. Geochemical and biological aspects of sulfide mineral dissolution: lessons from Iron Mountain. California. *Chem. Geol.* 169, 383–397.

Evangelou, V.P., Zhang, Y.L., 1995. A review-pyrite oxidation mechanisms and acid mine drainage prevention. Crit. Rev. Environ. Sci. Technol. 25, 141–199.

Felmy, A.R., Xia, Y., Wang, Z., 2005. The solubility product of $NaUO_2PO_4xH_2O$ determined in phosphate and carbonate solutions. Radiochim. Acta 93, 401–408.

Fesenko, S., Carvalho, F., Martin, P., Moore, W.S., Yankovic, T., 2014. Radium in the environment. The Environmental Behaviour of Radium: Revised Edition. IAEA, Vienna, Austria, pp. 33–105.

Finch, R., Murakami, T., 1999. Systematics and paragenesis of uranium minerals. In: Burns, P.C., Finch, R. (Eds.), Uranium: Mineralogy, Geochemistry and the Environment, 38 Reviews in Mineralogy. Mineralogical Society of America, Washington, D.C, pp. 91–179.

Forbes, P., 1989. Roˆles des structures sédimentaires et tectoniques, du volcanisme alcalin régional et des fluides diagénétiques - hydrothermaux pour la formation des minéralisations à U-Zr-Zn-V-Mo d'Akouta (Niger). Université de Bourgogne.

Fuller, C.C., Bargar, J.R., Davis, J.A., Piana, M.J., 2002. Mechanisms of uranium interactions with hydroxyapatite: implications for groundwater remediation. Environ. Sci. Technol. 36 (2), 158–165.

Fuchs, L.H., Gebert, E., 1958. X-ray studies of synthetic coffinite, thorite, and uranthorite. Am. Mineral. 43, 243–248.

Gorman-Lewis, D., Burns, P.C., Fein, J.B., 2008. Review of uranyl mineral solubility measurements. J. Chem. Thermodyn. 40, 335–352.

Grenthe, I., Drozdzynski, J., Fujino, T., Buck, E.C., Albrecht-Schmitt, T.E., Wolf, S.F., Uranium, 2006. In: Edelstein, N.M., Fuger, J., Morss, L.R. (Eds.), The Chemistry of the Actinide and Transactinide Elements, third ed., vol. 1. Springer, Dordrecht, pp. 253–698. Chap. 5.

Grenthe, I., Fuger, J., Konings, R.J.M., Lemire, R.J., Muller, A.B., Nguyen-Trung Cregu, C., Wanner, H., 1992. Chemical Thermodynamics of Uranium. Elsevier, New York.

Grenthe, I., Lagerman, B., 1993. Ternary metal complexes. 2. The U(VI)-SO_2^{-4}-OH^- system radiochim. Acta 61, 169–176.

Hennig, C., Ikeda, A., Schmeide, K., Brendler, V., Moll, H., Tsushima, S., Scheinost, A.C., Skanthakumar, S., Wilson, R., Soderholm, L., Servaes, K., Gorrler-Walrand, C., Van Deun, R., 2008. The relationship of monodentate and bidentate coordinated uranium (VI) sulfate in aqueous solution. Radiochim. Acta 96, 607–611.

Hennig, C, Schmeide, K, Brendler, V, Moll, H, Tsushima, S, Scheinost C, A, 2007. EXAFS investigation of U(VI), U(IV), and Th(IV) sulfato complexes in aqueous solution. Inorg. Chem. 5882–5892.

His, C.-K.D., Langmuir, D., 1985. Adsorption of uranyl onto ferric oxyhydroxides: application of the surface complexation site-binding model. Geochem. Cosmochim. Acta 49, 1931–1941.

Jamieson, H.E., 2011. Geochemistry and mineralogy of solid mine waste: essential knowledge for predicting environmental impact. Elements 7, 381–386.

Jensen, K.A., Palenik, C.S., Ewing, R.C., 2002. U6+ phases in the weathering zone of the Bangombé U-deposit: observed and predicted mineralogy. Radiochim. Acta 90, 761–769.

Jerden Jr., J.L., Sinha, A.K., 2006. Geochemical coupling of uranium and phosphorous in soils overlying an unmined uranium deposit: coles Hill, Virginia. J. Geochem. Explor. 91, 56–70.

Jerden Jr., J.L., Sinha, A.K., 2003. Phosphate based immobilization of uranium in an oxidizing bedrock aquifer. Appl. Geochem. 18, 823–843.

Jerden Jr., J.L., Sinha, A.K., Zelazny, L., 2003. Natural immobilization of uranium by phosphate mineralization in an oxidizing saprolite–soil profile: chemical weathering of the Coles Hill uranium deposit, Virginia. Chem. Geol. 199, 129–157.

Jin, Q., Su, L., Montavon, G., Sun, Y., Chen, Z., Guo, Z., Wu, W., 2016. Surface complexation modeling of U(VI) adsorption on granite at ambient/elevated temperature: experimental and XPS study. Chem. Geol. 433, 81–91.

Johnson, D.B., Hallberg, K.B., 2005. Acid mine drainage remediation options: a review. Sci. Total Environ. 338, 3–14.

Kelly, S.D., 2010. Chapter 14 - uranium chemistry in soils and sediments. Dev. Soil Sci. 34, 411–466.

King, P.T., Michel, J., Moore, W.S., 1982. Ground water geochemistry of 228Ra, 226Ra and 222Rn. Geochem. Cosmochim. Acta 46, 1173–1182.

Krivovichev, S., Plàsil, J., 2013. Chapter 3: mineralogy and crystallography of uranium. Uranium Cradle to the Grave. Mineralogical Association of Canada.

Lahrouch, F., Guo, N., Hunault, M.O.J.Y., Solari, P.L., Descostes, M., Gerard, M., 2021. Uranium retention on iron oxyhydroxides in post-mining environmental conditions. Chemosphere 128473.

Langmuir, D., 1978. Uranium solution-mineral equilibria at low temperatures with applications to sedimentary ore deposits. Geochem. Cosmochim. Acta 42, 547–569.

Lee, J.-K., Baik, M.-H., Choi, J.-W., Seo, M.-S., 2011. Development of a web-based sorption database (KAERI-SDB) and application to the safety assessment of a radioactive waste disposal. Nucl. Eng. Des. 241, 5316–5324.

Lin, J., Sun, W., Desmarais, J., Chen, N., Feng, R., Zhang, P., Li, D., Lieu, A., Tse, J.S., Pan, Y., 2018. Uptake and speciation of uranium in synthetic gypsum ($CaSO_4$•$2H_2O$): applications to radioactive mine tailings. J. Environ. Radioact. 181, 8–17.

Locock J, Andrew, Burns C, Peter, 2002. The crystal structure of triuranyl diphosphate tetrahydrate. J. Solid State Chem. 163, 275–280.

Locock, A.J., Burns, P.C., Flynn, T.M., 2005. The role of water in the structures of synthetic hallimondite, $Pb_2[(UO_2)(AsO_4)_2](H_2O)_n$ and synthetic parsonsite, $Pb_2[(UO_2)(PO4)_2](H_2O)_n$, $0<n<0.5$. Am. Mineral. 90, 240–246.

Lottering, M.J., Lorenzen, L., Phala, N.S., Smit, J.T., Schalkwyk, G.A.C., 2008. Mineralogy and uranium leaching response of low grade South African ores. Miner. Eng. 1, 16–22.

Martin, G.R., Tuck, D.G., 1959. The specific activity of radium. Int. J. Appl. Radiat. Isot. 5, 141–145.

Molinari, J., Snodgrass, W.J., 1990. The chemistry and radiochemistry of radium and the other elements of the uranium and thorium natural decay series. In: The Environmental Behaviour of Radium, IAEA Technical Report Series No. 310, ume 1. IAEA, Vienna, Austria, ISBN 92-0-125090-8, pp. 11–56.

Moll, H., Reich, T., Hennig, C., Rossberg, A., Szabó, Z., Grenthe, I., 2000. Solution coordination chemistry of uranium in the binary UO_2^{2+}-SO_4^{2} and the ternary UO_2^{2+}-SO_4^{2} -OH system. Radiochim. Acta 88, 559–566.

Morin, G., Calas, G., 2006. Arsenic in soils, mine tailings, and former industrial sites. Elements 2, 97–101.

Morosin, B., 1978. Hydrogen uranyl phosphate tetrahydrate, a hydrogen ion solid electrolyte. Acta Crystallogr. B 34, 3732–3734.

Murakami, T., Ohnuki, T., Isobe, H., Sato, T., 1997. Mobility of uranium during weathering. Am. Mineral. 82, 888–899.

Murakami, T., Sato, T., Ohnuki, T., Isobe, H., 2005. Field evidence for uranium nanocrystallization and its implications for uranium transport. Chem. Geol. 221, 117–126.

Nirdosh, I., Muthuswami, S.V., Baird, M.H.I., 1984. Radium in uranium mill tailing – some observations on retention and removal. Hydrometallurgy 12, 151–176.

Pagel, M., Cavellec, S., Forbes, P., Gerbaud, O., Vergely, P., Wagani, I., Mathieu, M., 2005. Uranium deposits in the Arlit area (Niger). Mineral Deposit Research: Meeting the Global Challenge 303–305.

Park, I., Tabelin, C.B., Jeon, S., Li, X., Seno, K., Ito, M., Hiroyosh, N., 2019. A review of recent strategies for acid mine drainage prevention and mine tailings recycling. Chemosphere 219, 588–606.

Payne, T.E., Davis, J.A., Waite, T.D., 1996. Uranium adsorption on ferrihydrite - effects of phosphate and humic acid. Radiochim. Acta 74, 239–243.

Plášil, J., Kampf, A.R., Kasatkin, A.V., Marty, J., Škoda, R., Silva, S., Čejka, J., 2013. Meisserite, $Na_5(UO_2)(SO_4)_3(SO_3OH)(H_2O)$, a new uranyl sulfate mineral from the Blue lizard mine, san juan county, Utah, USA. Mineral. Mag. 77, 2975–2988.

Rai, D., Xia, Y., Rao, L., Hess, N.J., Felmy, A.R., Moore, D.A., McCready, D.E., 2005. Solubility of $(UO_2)_3(PO_4)_2\ 4H_2O$ in H^+ - Na^+ - OH - $H_2PO^-_4$ - HPO^{2-}_4 - PO^{3-}_4 - H_2O and its comparison to the analogous PuO^{2+}_2 system. J. Solut. Chem. 34, 469–498.

Ravel, B., Newville, M., 2005. IUCr ATHENA, ARTEMIS, HEPHAESTUS: data analysis for X-ray absorption spectroscopy using IFEFFIT. J. Synchrotron Radiat. 12, 537–541.

Rehr, J.J., Kas, J.J., Vila, F., Prange, D.M.P., Jorissen, K., 2010. Parameter-free calculations of X-ray spectra with FEFF9. Phys. Chem. Chem. Phys. 12, 5503–5513.

Robertson, J, Hendry J, M, Kotzer, T, Hughes A, K, 2019. Geochemistry of uranium mill tailings in the Athabasca Basin Saskatchewan, Canada: A review. Crit. Rev. Environ. Sci. Technol. 1237–1293.

Rothe, J., Butorin, S., Dardenne, K., Denecke, M.A., Kienzler, B., Loble, M., Metz, V., Seibert, A., Steppert, M., Vitova, T., Walther, C., Geckeis, H., 2012. The INE-beamline for actinide science at ANKA. Rev. Sci. Instrum. 83, 043105.

Schindler, M., Durocher, J.L., Kotzer, T.G., Hawthorne, F.C., 2012. Uranium-bearing phases in a U-mill disposal site in Northern Canada: products of the interaction between leachate/raffinate and tailings material. Appl. Geochem. 29, 151–161.

Sharifironizi, M., Burns, P.C., 2018. Investigation of the structural stability of zippeite-group minerals using high-temperature calorimetry. Can. Mineral. 56, 7–14.

Shock, E.L., Sassani, D.C., Betz, H., 1997. Uranium in geologic fluids - estimates of standard partial molal properties, oxidation potentials, and hydrolysis constants at high temperatures and pressures *Geochim.* Cosmochim. Acta 61, 4245–4266.

Singh, A., Ulrich, K.-U., Giammar, D.E., 2010. Impact of phosphate on U(VI) immobilization in the presence of goethite. Geochem. Cosmochim. Acta 74, 6324–6343.

Sowder, A.G., Clark, S.B., Fjeld, R.A., 2001. The impact of mineralogy in the U(VI)-Ca-PO4 system on the environmental availability of uranium. J. Radioanal. Nucl. Chem. 248, 517–524.

Steinhausler, F., Zaitseva, L., 2007. Uranium mining and milling: material security and risk assessment. Int. J. Nucl. Govern. Econ. Ecol 1, 286–304.

Szymanski, J.T., Scott, J.D., 1982. A crystal-structure refinement of synthetic brannerite, UTi2O6, and its bearing on rate of alkaline-carbonate leaching of brannerite in ore. Can. Mineral. 20, 271–279.

Tayal, A, Conradson D, S, Kanzari, A, Lahrouch, F, Descostes, M, Gérard, M, 2019. Uranium speciation in weathered granitic waste rock piles: an XAFS investigation. RSC Adv. 9, 11762–11773.

Thompson, H.A., Brown, G.E., Parks, G.A., 1997. XAFS spectroscopic study of uranyl coordination in solids and aqueous solution. Am. Mineral. 82, 483–496.

Vazquez, G.J., Dodge, C.J., Francis, A.J., 2007. Interactions of uranium with polyphosphate. Chemosphere 70, 263–269.

Wellman, D.M., 2006. Effects of pH, temperature, and aqueous organic material on the dissolution kinetics of meta-autunite minerals, $(Na,Ca)_2$-1$[(UO_2)(PO_4)]_2.3H_2O$. Am. Mineral. 91, 143–158.

Wellman, D.M., McNamara, B.K., Bacon, D.H., Cordova, E.A., Ermi, R.M., Top, L.M., 2009. Dissolution kinetics of meta-torbernite under circum-neutral to alkaline conditions. Environ. Chem. 6, 551–560.

Willard, R.L., Campbell, T.J., Rapp, G.R., 1990. Encyclopedia of Minerals, 2nd Ed. New York. Chapman & Hall, London. Van Nostrand Reinhold.